Available online at www.sciencedirect.com
SCIENCE DIRECT®
PERGAMON
International Journal of Multiphase Flow 29 (2003) 1153–1182
International Journal of Multiphase Flow
www.elsevier.com/locate/ijmulflow

A model for turbulent polydisperse two-phase flow in vertical channels

M.S. Politano [a,b,*], P.M. Carrica [b], J. Converti [a]

[a] *Instituto Balseiro Av. Bustillo km. 9.5, 8400 Bariloche, Argentina*
[b] *Iowa Institute of Hydraulic Research, The University of Iowa, Iowa City, IA 52242, USA*

Received 15 August 2002; received in revised form 2 April 2003

Abstract

A polydisperse two-phase flow model is developed and used to analyze the effect of the bubble size on the radial phase distribution in vertical upward channels. The two-fluid model is evaluated considering that the bubble size distribution can be represented with groups of constant mass. The model accounts for interfacial momentum transfer terms arising from drag, lift, turbulent dispersion and wall forces for the different bubble sizes. The turbulence is modeled with the k–ε model for bubbly flow. A two-phase wall logarithmic law is developed to evaluate the boundary conditions for the k–ε and the two-fluid models. The turbulence in the buffer and laminar near-wall regions is evaluated considering the asymptotic consistency of the k–ε model approaching the solid surface. The model is able to predict the transition from the near-wall gas volume fraction peaking to the core peaking beyond a critical bubble size. The double gas volume fraction peak experimentally observed when both, small and big bubbles, are present can be also simulated. The model was numerically solved for fully developed flow by means of a finite difference method and the results were compared against the experimental data measured by others in air/water vertical ducts.

Keywords: Two-phase flow; Phase distribution; Polydisperse bubbly flow; k–ε two-phase boundary conditions

1. Introduction

Turbulent bubbly gas/liquid flow in ducts occurs in many applications in diverse industries such as chemical, pharmaceutical, food and power, among others. The prediction of the phase

* Corresponding author. Address: Iowa Institute of Hydraulic Research, The University of Iowa, Iowa City, IA 52242, USA. Tel.: +1-319-3355-638; fax: +1-319-335-5238.
E-mail address: mspolitano@mail.iihr.uiowa.edu (M.S. Politano).

0301-9322/03/$ - see front matter
doi:10.1016/S0301-9322(03)00065-X

velocities and distribution in the ducts is of paramount importance for the correct design of the duct and for the prediction of the pressure drop.

Many experimental and numerical studies have been published related to the phase distribution in steady-state, fully-developed flows in vertical ducts. Serizawa et al. (1975a,b) conducted an exhaustive experimental study of the air/water flow in a vertical duct. The authors measured the radial distribution of gas volume fraction, gas and liquid velocities and the turbulence structure at different gas superficial velocities. Although they report the transition from bubbly to the slug flow pattern, they inform that the range of mean bubble diameters in their experimental study was approximately 4 mm. The authors report bubble diameters for bubbly flow but they do not inform any bubble size measurement in the bubble-to-slug transition or for slug flow. Wang et al. (1987) analyzed air/water flows studying, specially, the effects of the presence of gas bubbles on the turbulence of the liquid. The authors do not give any information about the bubble size distribution. Even at similar reported experimental conditions, there is substantial disagreement between the experimental data of Serizawa et al. (1975a,b) and Wang et al. (1987).

The first reference to the effect of bubble size in the phase distribution in a vertical channel appears to be due to Sekoguchi et al. (1974), as mentioned by Liu (1997). They found that small bubbles are attracted toward the wall, while bubbles larger than about 5 mm rise in the core of the duct.

Zun (1988, 1990) measured radial distribution of the gas volume fraction in a channel using a bubble injector specially designed to control the bubble size. In the experiences, the bubble size was maintained constant for low superficial gas velocities to prevent bubble coalescence and breakup. The results show that the bubble size can be the key parameter to explain the differences found between the experimental data of Serizawa et al. (1975a,b) and Wang et al. (1987).

Liu (1991) designed an experiment to observe the effect of the bubble size distribution on the phase radial distribution. The author measured the radial profiles of gas volume fraction, bubble impact rate and bubble mean diameter, for different gas and liquid superficial velocities. Liu and Bankoff (1993a,b) measured the radial profiles of gas and liquid velocities and the turbulence structure for mean bubble diameters ranging from 2 to 4 mm. In recent works, Liu (1997, 1998), and Liu and Wang (2001) complement the study of Liu (1991) measuring radial profiles of turbulent fluctuations, shear stress at the wall and interfacial area concentration.

Some numerical studies were carried out to predict the phase radial distribution in ducts. Antal et al. (1991) developed a model based in the two-fluid approach (Ishii, 1975; Drew and Lahey, 1979) for laminar flow. Lopez de Bertodano et al. (1994) measured profiles of liquid velocity and gas volume fraction in a duct of triangular section and used the two-fluid model to calculate the turbulent two-phase flow. The model assumes that the turbulence induced by the bubbles can be added linearly to the shear induced turbulence. Besides, the two-phase turbulent viscosity is calculated by linear superposition of the shear induced and bubble induced turbulent viscosities. None of the above-mentioned models can predict the convex shape of the gas volume fraction profile for big bubbles in upward flow since they used a constant positive lift coefficient. Troshko and Hassan (2001a,b) present a two-phase flow model that includes the near wall region and develop a two-phase wall law. The described models rely on the assumption of monodisperse flow, so they are unable to match the phase distribution found with flows formed with bubbles of different sizes.

In this work we develop a model for turbulent polydisperse two-phase flows. The formulation uses the two-fluid model and the k–ε model for two-phase flow (Lahey and Drew, 1999) to represent the turbulence.

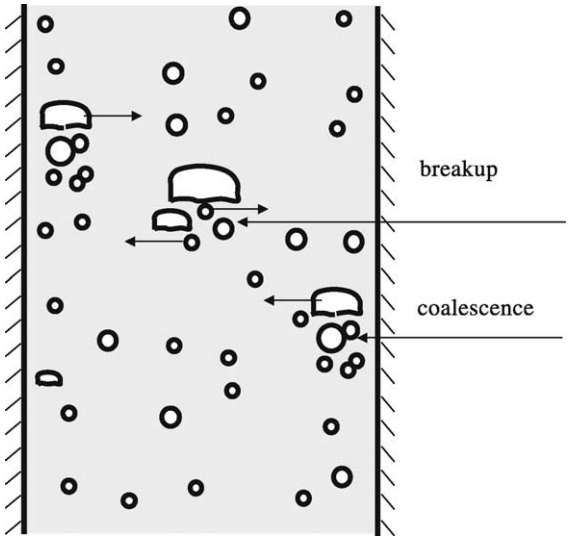

Fig. 1. Breakup and coalescence process in a vertical channel.

Such as is shown schematically in Fig. 1, in a steady-state, fully-developed flow condition, there is an equilibrium of bubbles breakup and coalescence that results in a given bubble size distribution. Near the wall, the high gas volume fraction due to the accumulation of small bubbles will tend to coalesce forming larger bubbles that tend to travel to the center of the channel if they can survive breakup caused by the high shear stress and turbulence intensity. At the center of the channel, larger bubbles can breakup and the resulting small bubbles will tend to migrate to the wall. In this paper we neglected this breakup and coalescence process; therefore it is only applicable to flows in which the gas and liquid superficial velocities are low enough so that both the coalescence and breakup are also negligible, though some experimental results indicate that even at low flow rates the phenomena might be important.

The wall logarithmic law, valid for single-phase flows in the near-wall region, was corrected for two-phase flows by means of a simplified model as first approximation. The near-wall turbulence was solved studying the asymptotic consistency of the properties approaching the surface.

The polydisperse bubble population was solved using a multigroup approach (Carrica et al., 1999). The two-phase equations were numerically solved for steady-state, fully-developed flow using the method of finite differences.

2. Mathematical model

2.1. Two-fluid model

2.1.1. Mass conservation

The continuity equation of the two-fluid model for flows with no interfacial mass transfer is (Ishii, 1975; Drew and Lahey, 1979):

$$\frac{\partial(\rho_k \varepsilon_k)}{\partial t} + \nabla \cdot (\rho_k \vec{u}_k \varepsilon_k) = 0 \tag{1}$$

where ε is the gas volume fraction, ρ is the density constant within each phase and $\vec{u}$ is the velocity. The subscripts k = l or g denotes the liquid or gas phase.

We assume that the disperse phase can be represented by N groups of constant mass (Carrica et al., 1999). Using this multigroup approach and assuming that the coalescence and breakup are negligible, Eq. (1) represents the continuity equation for bubble group-g. Eq. (1) applied to steady-state, fully-developed flow, results in no radial flow:

$$u_{r,k} = 0 \tag{2}$$

where $u_{r,k}$ is the averaged radial velocity of phase or group k.

2.1.2. Momentum conservation

The momentum equation for the phase or group k, with no break-up or coalescence, is (Ishii, 1975; Drew and Lahey, 1979; Carrica et al., 1999):

$$\begin{aligned}\frac{\partial(\rho_k \varepsilon_k \vec{u}_k)}{\partial t} + \nabla \cdot (\rho_k \varepsilon_k \vec{u}_k \vec{u}_k) = {} & -\varepsilon_k \nabla p_k + \rho_k \varepsilon_k \vec{g} + \vec{M}_k + \varepsilon_k \nabla(\boldsymbol{\sigma}_k^{\mathrm{Re}} + \boldsymbol{\tau}_k) \\ & + [(\boldsymbol{\sigma}_k^{\mathrm{Re}} - \boldsymbol{\sigma}_{\mathrm{i}}^{\mathrm{Re}}) + (\boldsymbol{\tau}_k - \boldsymbol{\tau}_{\mathrm{i}})]\nabla \varepsilon_k - (p_k - p_{\mathrm{i}})\nabla \varepsilon_k\end{aligned} \tag{3}$$

where $\vec{M}_k$ is the interfacial force calculated with averaged variables, $\boldsymbol{\tau}_k$ and $\boldsymbol{\sigma}_k^{\mathrm{Re}}$ are the viscous shear and Reynolds stress tensors, respectively, $\vec{g}$ is the gravity acceleration and p is the pressure. The subscripts i indicate that the variables must be evaluated at the interface. For steady-state, fully-developed flow, and using Eq. (1), Eq. (3) results:

$$0 = -\varepsilon_k \nabla p_k + \rho_k \varepsilon_k \vec{g} + \vec{M}_k + \varepsilon_k \nabla(\boldsymbol{\sigma}_k^{\mathrm{Re}} + \boldsymbol{\tau}_k) + [(\boldsymbol{\sigma}_k^{\mathrm{Re}} - \boldsymbol{\sigma}_{\mathrm{i}}^{\mathrm{Re}}) + (\boldsymbol{\tau}_k - \boldsymbol{\tau}_{\mathrm{i}})]\nabla \varepsilon_k - (p_k - p_{\mathrm{i}})\nabla \varepsilon_k \tag{4}$$

2.2. Constitutive equations

At this point closure laws are required for the interfacial force, $\vec{M}_k$, and the stress tensors, $(\boldsymbol{\sigma}_k^{\mathrm{Re}} + \boldsymbol{\tau}_k)$.

In the gas momentum equation the stress terms are smaller than the pressure gradient and interfacial force terms, so usually they are neglected (Antal et al., 1991; Lopez de Bertodano et al., 1994). In addition, the pressure in the gas phase is similar to the pressure at the interface, resulting $(p_{\mathrm{g}} - p_{\mathrm{i}}) \approx 0$.

In the liquid momentum equation, we assume that the difference between the interfacial stress tensors and the stress tensors in the liquid phase, $(\boldsymbol{\sigma}_{\mathrm{l}}^{\mathrm{Re}} - \boldsymbol{\sigma}_{\mathrm{i}}^{\mathrm{Re}})$ and $(\boldsymbol{\tau}_{\mathrm{l}} - \boldsymbol{\tau}_{\mathrm{i}})$, are smaller than the other terms. A similar hypothesis was adopted by Lopez de Bertodano et al. (1994).

2.2.1. Interfacial momentum

For steady-state, fully-developed flow, the interfacial force can be partitioned into four main terms: drag, lift, wall force and turbulent dispersion:

$$\vec{M}_{\mathrm{g}} = \vec{M}_{\mathrm{g}}^{\mathrm{D}} + \vec{M}_{\mathrm{g}}^{\mathrm{l}} + \vec{M}_{\mathrm{g}}^{\mathrm{w}} + \vec{M}_{\mathrm{g}}^{\mathrm{TD}} \tag{5}$$

2.2.1.1. Drag force. The drag force per unit volume, $\vec{M}_g^D$, for spherical bubbles of group-g was modeled by Ishii and Zuber (1979) as:

$$\vec{M}_g^D = -\frac{3}{8}\varepsilon_g \rho_l \frac{C_g^D}{r_g}\vec{u}_{R_g}|\vec{u}_{R_g}| \tag{6}$$

where r_g is the radius of bubbles of group-g, $\vec{u}_{R_g}$ is the relative velocity between the bubbles of group-g and the liquid phase and C_g^D is the drag coefficient for which many correlations are available (Ishii and Zuber, 1979; Ishii and Mishima, 1984; Tomiyama, 1998). The experimental data used in this paper correspond mostly with conditions in churn–turbulent regime, in which the flow becomes agitated and there is a significant bubble–bubble interaction by wake entrainment. We found that the experimental results were best adjusted by the correlation of Ishii and Zuber (1979) for the churn–turbulent regime, in which the drag coefficient is independent of the bubble size and is given by:

$$C_g^D = C^D = \tfrac{8}{3}\varepsilon_l^2 \tag{7}$$

2.2.1.2. Lift force. The lift force, $\vec{M}_g^l$, can be written as (Drew and Lahey, 1979):

$$\vec{M}_g^l = -\varepsilon_g \rho_l C_g^l \vec{u}_{R_g} \times (\nabla \times \vec{u}_l) \tag{8}$$

In Eq. (8), the lift coefficient of a bubble of group-g, C^l, can be expressed as (Tomiyama, 1998):

$$C_g^l \begin{cases} \min[0.288\tanh(0.121Re_g); 0.00105Eo_{d_g}^3 - 0.0159Eo_{d_g}^2 - 0.0204Eo_{d_g} + 0.474] & \text{if } Eo_g < 4 \\ 0.00105Eo_{d_g}^3 - 0.0159Eo_{d_g}^2 - 0.0204Eo_{d_g} + 0.474 & \text{if } 4 \leqslant Eo_g \leqslant 10 \\ -0.29 & \text{if } Eo_g > 10 \end{cases} \tag{9}$$

where $Re_g = \rho_l \vec{u}_{R_g} 2r_g/\mu_l$ is the Reynolds number and $Eo_g = (g(\rho_l - \rho_g)4r_g^2)/\sigma$ is the Eötvos number, with μ the liquid molecular viscosity and σ the interfacial tension. The modified Eötvos number of bubbles of group-g is:

$$Eo_{d_g} = \frac{g(\rho_l - \rho_g)d_H^2}{\sigma} \tag{10}$$

with d_H the maximum bubble horizontal dimension. The ratio between the spherical bubble diameter and the maximum horizontal dimension of a spheroid bubble, for bubbles of equal mass, is given by:

$$W = \left(\frac{2R_g}{d_H}\right)^3 \tag{11}$$

where W is evaluated with the empirical correlation of Wellek et al. (1966):

$$W = (1 + 0.163Eo^{0.757})^{-1} \tag{12}$$

Notice that with Tomiyama's correlation the lift coefficient changes sign for a bubble diameter of 5.6 mm. Also, note that the widely used lift coefficient of 0.1 is attained for a bubble radius of about 2.6 mm.

2.2.1.3. Wall force. The model proposed by Antal et al. (1991) to explain the force that a wall exerts on the disperse phase, $\vec{M}_{\mathrm{g}}^{\mathrm{w}}$, is:

$$\vec{M}_{\mathrm{g}}^{\mathrm{w}} = \left(C_{\mathrm{w1}} + C_{\mathrm{w2}} \frac{r_{\mathrm{g}}}{y} \right) \varepsilon_{\mathrm{g}} \rho_{\mathrm{l}} \frac{\vec{u}_{R_{\mathrm{g}}}^2}{r_{\mathrm{g}}} \vec{n}_{\mathrm{w}} \tag{13}$$

where y is the distance from the wall, $\vec{n}_{\mathrm{w}}$ is the outward normal to the wall and the model constants are $C_{\mathrm{w1}} = -0.1$ and $C_{\mathrm{w2}} = 0.147$. Eq. (13) was corrected by Tomiyama (1998) to avoid the attraction force by the wall predicted for large y:

$$\vec{M}_{\mathrm{g}}^{\mathrm{w}} = 0 \quad \text{if } y > \frac{C_{\mathrm{w2}}}{C_{\mathrm{w1}}} r_{\mathrm{g}} \tag{14}$$

2.2.1.4. Turbulent dispersion. The turbulent dispersion, $\vec{M}_{\mathrm{g}}^{\mathrm{TD}}$, was modeled by Carrica et al. (1999) as:

$$\vec{M}_{\mathrm{g}}^{\mathrm{TD}} = -\frac{3}{8} \rho_{\mathrm{l}} v^{\mathrm{t}} \frac{C^{\mathrm{D}}}{r_{\mathrm{g}}} |\vec{u}_{R_{\mathrm{g}}}| \nabla \varepsilon_{\mathrm{g}} \tag{15}$$

where v^{t} is the turbulent viscosity.

2.2.2. Molecular stress tensor

The viscous shear stress tensor in the liquid phase is given by:

$$\boldsymbol{\tau}_{\mathrm{l}} = \rho_{\mathrm{l}} v (\nabla \vec{u}_{\mathrm{l}} + \nabla \vec{u}_{\mathrm{l}}^{T}) \tag{16}$$

where v is the liquid molecular cinematic viscosity.

2.2.3. Turbulent stress tensors

The Reynolds stress tensor for the liquid phase can be written as:

$$\boldsymbol{\sigma}_{\mathrm{l}}^{\mathrm{Re}} = \rho_{\mathrm{l}} [v^{\mathrm{t}} (\nabla \vec{u}_{\mathrm{l}} + \nabla \vec{u}_{\mathrm{l}}^{T}) - \tfrac{2}{3} k \mathbf{I}] + \boldsymbol{\sigma}_{\mathrm{l}}^{\mathrm{b}} \tag{17}$$

where k is the turbulent kinetic energy and $\boldsymbol{\sigma}_{\mathrm{l}}^{\mathrm{b}}$ is the turbulence induced stress due to the motion of the liquid around the bubbles. k is modeled using the k–ε model for two-phase flows (Lahey and Drew, 1999):

$$\varepsilon_{\mathrm{l}} \frac{\mathrm{d}k}{\mathrm{d}t} + \varepsilon_{\mathrm{l}} \vec{u}_{\mathrm{l}} \nabla k = \nabla \cdot (\varepsilon_{\mathrm{l}} \boldsymbol{v}^{\mathrm{t}} \nabla k) + P_{\mathrm{l}} - \varepsilon_{\mathrm{l}} \varepsilon + \varepsilon_{\mathrm{l}} \phi_k \tag{18}$$

where the turbulence production rate, P_{l}, is:

$$P_{\mathrm{l}} = \varepsilon_{\mathrm{l}} v^{\mathrm{t}} (\nabla \vec{u}_{\mathrm{l}} + \nabla \vec{u}_{\mathrm{l}}^{T}) : \nabla \vec{u}_{\mathrm{l}} \tag{19}$$

the turbulent dissipation rate, ε, is given by:

$$\varepsilon_{\mathrm{l}} \frac{\mathrm{d}\varepsilon}{\mathrm{d}t} + \varepsilon_{\mathrm{l}} \vec{u}_{\mathrm{l}} \nabla \varepsilon = \nabla \cdot \left(\frac{\varepsilon_{\mathrm{l}} \boldsymbol{v}^{\mathrm{t}}}{\sigma_{\varepsilon}} \nabla \varepsilon \right) + C_{\varepsilon 1} P_{\mathrm{l}} \frac{\varepsilon}{k} - \varepsilon_{\mathrm{l}} C_{\varepsilon 2} \frac{\varepsilon^2}{k} + \alpha_{\mathrm{l}} \phi_k C_{\varepsilon 2} \frac{\varepsilon}{k} \tag{20}$$

and the bubble-induced turbulence source, ϕ_k, is (Lee et al., 1989):

$$\phi_k = C_p \sum_{g=1}^{N} \frac{\varepsilon_g |\vec{u}_{R_g}|^3}{2r_g} \tag{21}$$

with $C_p = 0.25$ for non-interacting spherical bubbles. For non-spherical bubbles C_p is larger. Applying potential flow to a spheroid bubble moving in helical path in water, the range of C_p can be extended to (Lopez de Bertodano et al., 1994):

$$0.5 < C_p < 0.7 \tag{22}$$

If the effect of a wake is considered these numbers could be even bigger. In the wall region the bubbles are deformed and it is possible that the wake effects became more important due to the concentration of small bubbles in this zone. Unfortunately, there are not models available that consider all these effects together. In this work we adopted $C_p = 1$. It is possible to note that, for the experimental conditions used, Eq. (21) with $C_p = 1$ give similar results to the model proposed by Troshko and Hassan (2001a) for the bubble turbulence source.

Due to the lack of additional information for two-phase flows, and because the model must reduce to the k–ε model for single-phase flows when the gas volume fraction tends to zero, the constants $C_{\varepsilon 1}$, $C_{\varepsilon 2}$, σ_ε are taken to be the same as in the standard k–ε model for single-phase flow: $C_{\varepsilon 1} = 1.44$, $C_{\varepsilon 2} = 1.92$ and $\sigma_\varepsilon = 1.3$. The turbulent viscosity is expressed by:

$$\nu^t = C_\mu \frac{k^2}{\varepsilon} \tag{23}$$

where $C_\mu = 0.09$.

The bubble induced turbulence was modeled using potential flow around a bubble (Nigmatulin, 1979; Drew and Passman, 1998):

$$\boldsymbol{\sigma}_l^b = -\rho_l \frac{1}{20} \sum_{g=1}^{N} \varepsilon_g [\vec{u}_{R_g} \vec{u}_{R_g} + 3\vec{u}_{R_g} \cdot \vec{u}_{R_g} \mathbf{I}] \tag{24}$$

2.2.4. Jump conditions

The jump interfacial condition for a system with no mass transfer and neglecting surface tension, reduces to:

$$\vec{M}_l + \sum_{g=1}^{N} \vec{M}_g = 0 \tag{25}$$

The average pressure at the interface is smaller than the pressure in the liquid phase. Antal et al. (1991) and Lopez de Bertodano et al. (1994) modeled this effect using potential flow around a sphere (Lamb, 1932) and taking into account the contribution of all equal-size bubbles. For polydisperse flow we must to considerate the effect of the bubbles of different sizes, for this end we propose to weight the relative velocity with the gas volume fraction:

$$(p_i - p_l) = -C_p \rho_l \varepsilon_l \frac{\sum_{g=1}^{N} \varepsilon_g |\vec{u}_{R_g}|^2}{\sum_{g=1}^{N} \varepsilon_g} \tag{26}$$

3. Numerical method

3.1. Equations in cylindrical geometry

In order to outline the numerical method, the conservation equations, the constitutive relations and the jump conditions have been rewritten for steady-state, fully-developed flow in cylindrical geometry. It is important to note that the only non-zero term of the interfacial momentum in the axial direction is the drag force; while in the radial direction the lift, wall force and turbulent dispersion terms are important. In addition, according to Eq. (26), the axial pressure gradient for fully-developed flow is the same for gas and liquid phases.

Group-g gas—axial direction

$$0 = -\frac{\mathrm{d}p}{\mathrm{d}z} - \rho_{\mathrm{g}} g - \rho_{\mathrm{l}} \frac{3}{8} \frac{C^{\mathrm{D}}}{r_{\mathrm{g}}} |u_{R_{\mathrm{g}}}| u_{R_{\mathrm{g}}} \tag{27}$$

where $u_{R_{\mathrm{g}}}$ is the relative velocity between bubbles of group-g and the liquid phase, in the axial direction.

Group-g gas—radial direction

$$0 = -\varepsilon_{\mathrm{g}} \frac{\mathrm{d}p_{\mathrm{g}}}{\mathrm{d}r} - C_{\mathrm{g}}^{\mathrm{l}} \varepsilon_{\mathrm{g}} \rho_{\mathrm{l}} u_{R_{\mathrm{g}}} \frac{\mathrm{d}u_{\mathrm{l}}}{\mathrm{d}r} - \left(C_{\mathrm{w1}} + C_{\mathrm{w2}} \frac{r_{\mathrm{g}}}{y} \right) \frac{\varepsilon_{\mathrm{g}} \rho_{\mathrm{l}} |u_{R_{\mathrm{g}}}|^2}{r_{\mathrm{g}}} - \rho_{\mathrm{l}} \frac{3}{8} v^{\mathrm{t}} \frac{C^{\mathrm{D}}}{r_{\mathrm{g}}} |u_{R_{\mathrm{g}}}| \frac{\mathrm{d}\varepsilon_{\mathrm{g}}}{\mathrm{d}r} \tag{28}$$

Liquid phase—axial direction

$$0 = -\varepsilon_{\mathrm{l}} \frac{\mathrm{d}p}{\mathrm{d}z} - \varepsilon_{\mathrm{l}} \rho_{\mathrm{l}} g + \sum_{g=1}^{N} \varepsilon_{\mathrm{g}} \rho_{\mathrm{l}} \frac{3}{8} \frac{C^{\mathrm{D}}}{r_{\mathrm{g}}} |u_{R_{\mathrm{g}}}| u_{R_{\mathrm{g}}} + \varepsilon_{\mathrm{l}} \rho_{\mathrm{l}} \frac{1}{r} \frac{\mathrm{d}}{\mathrm{d}r} \left[r(\nu + \nu^{\mathrm{t}}) \frac{\mathrm{d}u_{\mathrm{l}}}{\mathrm{d}r} \right] \tag{29}$$

Liquid phase—radial direction

$$\begin{aligned} 0 = {} & -\varepsilon_{\mathrm{l}} \frac{\mathrm{d}p_{\mathrm{l}}}{\mathrm{d}r} + \sum_{g=1}^{N} \left[C_{\mathrm{g}}^{\mathrm{l}} \varepsilon_{\mathrm{g}} \rho_{\mathrm{l}} u_{R_{\mathrm{g}}} \frac{\mathrm{d}u_{\mathrm{l}}}{\mathrm{d}r} + \left(C_{\mathrm{w1}} + C_{\mathrm{w2}} \frac{r_{\mathrm{g}}}{y} \right) \frac{\varepsilon_{\mathrm{g}} \rho_{\mathrm{l}} |u_{R_{\mathrm{g}}}|^2}{r_{\mathrm{g}}} + \rho_{\mathrm{l}} \frac{3}{8} v^{\mathrm{t}} \frac{C^{\mathrm{D}}}{r_{\mathrm{g}}} |u_{R_{\mathrm{g}}}| \frac{\mathrm{d}\varepsilon_{\mathrm{g}}}{\mathrm{d}r} \right] \\ & - \varepsilon_{\mathrm{l}} \rho_{\mathrm{l}} \left(\frac{2}{3} k \right) - \frac{3}{20} \varepsilon_{\mathrm{l}} \sum_{g=1}^{N} u_{R_{\mathrm{g}}}^2 \frac{\mathrm{d}\varepsilon_{\mathrm{g}}}{\mathrm{d}r} - \sum_{g=1}^{N} C_p (1 - \varepsilon_{\mathrm{g}}) \rho_{\mathrm{l}} |\vec{u}_{R_{\mathrm{g}}}|^2 \frac{\mathrm{d}\varepsilon_{\mathrm{l}}}{\mathrm{d}r} \end{aligned} \tag{30}$$

Adding Eq. (28) for all groups and Eq. (30), and using Eq. (26) and its derivative to evaluate the liquid radial pressure gradient, the gas radial pressure gradient results:

$$\begin{aligned} \frac{\mathrm{d}p_{\mathrm{g}}}{\mathrm{d}r} = {} & -\frac{2}{3} \varepsilon_{\mathrm{l}} \rho_{\mathrm{l}} \frac{\mathrm{d}k}{\mathrm{d}r} - \frac{3}{20} \varepsilon_{\mathrm{l}} \sum_{g=1}^{N} u_{R_{\mathrm{g}}}^2 \frac{\mathrm{d}\varepsilon_{\mathrm{g}}}{\mathrm{d}r} - \frac{C_p \varepsilon_{\mathrm{l}} \rho_{\mathrm{l}} \frac{\mathrm{d}\varepsilon_{\mathrm{l}}}{\mathrm{d}r}}{(1 - \varepsilon_{\mathrm{l}})^2} \sum_{g=1}^{N} u_{R_{\mathrm{g}}}^2 \varepsilon_{\mathrm{g}} \\ & - \frac{C_p \varepsilon_{\mathrm{l}} \rho_{\mathrm{l}}}{(1 - \varepsilon_{\mathrm{l}})} \left(\frac{\mathrm{d}\varepsilon_{\mathrm{l}}}{\mathrm{d}r} \sum_{g=1}^{N} u_{R_{\mathrm{g}}}^2 \varepsilon_{\mathrm{g}} + 2\varepsilon_{\mathrm{l}} \sum_{g=1}^{N} u_{R_{\mathrm{g}}} \frac{\mathrm{d}u_{R_{\mathrm{g}}}}{\mathrm{d}r} \varepsilon_{\mathrm{g}} + \varepsilon_{\mathrm{l}} \sum_{g=1}^{N} u_{R_{\mathrm{g}}}^2 \frac{\mathrm{d}\varepsilon_{\mathrm{g}}}{\mathrm{d}r} \right) \end{aligned} \tag{31}$$

The k–ε model, for steady-state, fully-developed flow, reduces to:

$$0 = -\frac{1}{r}\frac{\mathrm{d}}{\mathrm{d}r}\left(r\varepsilon_{\mathrm{l}}\nu^{\mathrm{t}}\frac{\mathrm{d}k}{\mathrm{d}r}\right) + \varepsilon_{\mathrm{l}}\nu^{\mathrm{t}}\left(\frac{\mathrm{d}u_{\mathrm{l}}}{\mathrm{d}r}\right)^2 - \varepsilon_{\mathrm{l}}\varepsilon + \varepsilon_{\mathrm{l}}C_p\sum_{g=1}^{N}\frac{\varepsilon_{\mathrm{g}}|u_{R_{\mathrm{g}}}|^3}{2r_{\mathrm{g}}} \tag{32}$$

$$0 = -\frac{1}{r}\frac{\mathrm{d}}{\mathrm{d}r}\left(r\frac{\varepsilon_{\mathrm{l}}\nu^{\mathrm{t}}}{\sigma_\varepsilon}\frac{\mathrm{d}\varepsilon}{\mathrm{d}r}\right) + C_{\varepsilon 1}\varepsilon_{\mathrm{l}}\nu^{\mathrm{t}}\left(\frac{\mathrm{d}u_{\mathrm{l}}}{\mathrm{d}r}\right)^2\frac{\varepsilon}{k} - \varepsilon_{\mathrm{l}}C_{\varepsilon 2}\frac{\varepsilon^2}{k} + \varepsilon_{\mathrm{l}}C_p\frac{\varepsilon}{k}\sum_{g=1}^{N}\frac{\varepsilon_{\mathrm{g}}|u_{R_{\mathrm{g}}}|^3}{2r_{\mathrm{g}}} \tag{33}$$

3.2. Boundary conditions

For a given inlet bubble size distribution, the system of Eq. (27) are algebraic expressions for the average relative velocity between bubbles of group-g and the liquid. The system of Eq. (28), using Eq. (31) to evaluate the gas radial pressure gradient, is formed by first-order partial differential equations, and require one boundary condition for each group. For this analysis we adopted zero derivative in the center of the duct subject to the restriction imposed by the known gas superficial velocity:

$$j_{\mathrm{g}} = \frac{2\int_0^{R_{\mathrm{c}}} u_{\mathrm{g}}\varepsilon_{\mathrm{g}} r\,\mathrm{d}r}{R_{\mathrm{c}}^2} \tag{34}$$

where R_{c} is the radius of the pipe and u_{g} is the velocity of the bubbles of group-g. Eq. (29) is a second-order elliptic partial differential equation and needs two boundary conditions. The first condition selected is zero derivative in the center of the duct. The second condition must be a Dirichlet condition. In the study of laminar flow of Antal et al. (1991) the no slip condition in the wall is used. In our case, the no slip condition is not appropriate because the standard k–ε model is not valid in the near-wall region. Instead, the velocity is specified at some distance from the wall (Wilcox, 1998). Lopez de Bertodano et al. (1994) used the logarithmic law of the wall as in single phase flow. We noted that, when the single-phase wall law is used, the profiles of liquid velocity and gas volume fraction change markedly with the selected distance where the boundary conditions are introduced. Moreover, there is experimental evidence that the single-phase logarithmic law is not valid for turbulent two-phase flows: the results of Sato et al. (1981) show an evident discrepancy between the experimental velocity profile and the single-phase logarithmic law; Nakoryavok et al. (1996) observed that the turbulent fluctuations close to the wall are reduced in downward flow as compared to a single-phase turbulent flow.

Several attempts have been made in the past to modify the usual single-phase wall-law boundary conditions to account for the presence of bubbles. Marié et al. (1997) studied the turbulent structure of a bubbly boundary layer. The authors proposed a modified logarithmic wall law that fits adequately their experimental liquid velocity data for low gas volume fraction. The adjustable constants of their new wall law become function of the flow parameters. A two-phase logarithmic law was deduced by Troshko and Hassan (2001a) using Sato's model for the eddy diffusivity. The new law has an empirical function deduced to fit the experimental data of Marié et al. (1997). The two-phase and the single-phase logarithmic laws were compared against the experimental data of Sato et al. (1981) and Wang et al. (1987). In a latter work Troshko and Hassan (2001b), used a two-fluid model and a k–ε turbulence model with their two-phase logarithmic law to predict flows in ducts. The model was validated and compared against several experimental data (Serizawa et al., 1975a,b; Wang et al., 1987 and Liu, 1998).

In this work we prefer a simplified approach, in which a first order correction to the logarithmic law of the wall was introduced to account for two-phase flows assuming similar hypothesis to those in single-phase flows. As will be shown later, the proposed wall law is simple to implement and properly predicts the main features of the flows analyzed here, though tends to underpredict the shear stress at the wall.

3.3. Two-phase wall logarithmic law

In order to develop a two-phase logarithmic law we use the conservation equations with appropriated simplifications. In the logarithmic region the interfacial momentum transfer, molecular diffusion and the pressure gradient are small compared with the turbulent diffusion term, so Eq. (29) reduces to:

$$0 = \rho_l \frac{d}{dy}\left[\varepsilon_l \nu^t \frac{du_l}{dy}\right] \tag{35}$$

where the near-wall pipe curvature was neglected. Eq. (35) shows that the turbulent shear stress, $\tau_{xy} = \rho_l \varepsilon_l \nu^t du_l/dy$, is constant in the logarithmic region, therefore $\tau_w \cong \tau_{xy}$ in this region, with τ_w the shear stress at the wall. Furthermore, we assume that in the logarithmic region, the gas volume fraction and the turbulent kinetic energy are essentially constant. This approximation is very strong and is valid only in a small region near the wall since there is where the principal variations of the variables occur. The hypothesis of constant turbulent kinetic energy is also assumed in single-phase flow. In addition, assuming that the bubble source terms are smaller than the other terms of Eqs. (32) and (33), the k–ε model simplifies to:

$$0 = -\frac{d}{dy}\left(\varepsilon_l \boldsymbol{\nu}^t \frac{dk}{dy}\right) + \varepsilon_l \boldsymbol{\nu}^t \left(\frac{du_l}{dy}\right)^2 - \varepsilon_l \varepsilon \tag{36}$$

$$0 = -\frac{d}{dy}\left(\frac{\varepsilon_l \boldsymbol{\nu}^t}{\sigma_\varepsilon} \frac{d\varepsilon}{dy}\right) + C_{\varepsilon 1} \varepsilon_l \boldsymbol{\nu}^t \left(\frac{du_l}{dy}\right)^2 - \varepsilon_l C_{\varepsilon 2} \frac{\varepsilon^2}{k} \tag{37}$$

The solutions of Eqs. (35)–(37) are:

$$u_l = \frac{u_*}{\sqrt{\varepsilon_l}}\left(\frac{\ln y^+}{K} + b\right) \tag{38}$$

$$k = \frac{u_*^2}{\varepsilon_l \sqrt{C_\mu}} \tag{39}$$

$$\varepsilon = \frac{u_*^3}{\varepsilon_l^{3/2} K y} \tag{40}$$

where

$$y^+ = \frac{y u_* \rho_l}{\mu} \tag{41}$$

$$u_* = \sqrt{\frac{\tau_w}{\rho_l}} \tag{42}$$

with, $K = 0.435$ and $b = 5.4$. Eqs. (38)–(40) are the boundary conditions for Eqs. (29), (32) and (33). The distance from the wall in which the boundary conditions are set, y_{lim}, must satisfy $30 \leqslant y^+ \leqslant 100$. Similarly to the hypothesis adopted by Lahey and Drew (1999) to evaluate the constants of the k–ε model for two-phase flow and due to the lack of other evidence we assume that the constants of the logarithmic law and the distance from the wall are the same as those for single-phase flow.

At this point it should be noticed that to determine the gas volume fraction is necessary to model the turbulence in the buffer and laminar near-wall regions. To this end we analyzed the asymptotic consistency of the turbulence model near the wall in a similar fashion to the low Reynolds number turbulence models in single-phase flow (Wilcox, 1998). The near wall turbulence kinetic energy and dissipation can be written as:

$$k = C_k y^2 + \mathrm{O}(y^3) \tag{43}$$

$$\varepsilon = 2C_k \nu + \mathrm{O}(y) \tag{44}$$

The constant $C_k = u_*^2/(\sqrt{C_\mu}\varepsilon_l y_{\text{lim}}^2)$ was evaluated considering the boundary condition given by Eq. (39). So, in the near-wall region, k is given by Eq. (44) with $k = 0$ at the wall and ε is a constant given by Eq. (45).

3.4. Solution procedure

The equations of the model were discretized using a finite differences method. The matrices resulting from the discretization of Eqs. (29), (32) and (33) are tridiagonal. The system of non-linear equations was solved with several iterative processes. A flow chart of the solution procedure is shown in Fig. 2. Due to the very strong coupling between the equations, they were alternatively solved using initial seeds. A strong relaxation was necessary to attain convergence. The process was stopped when the norm L1 of the error in all variables was lower than 10^{-6}. To get these residuals the gas volume fraction error must be lower than 10^{-8}.

In the first process the gas/liquid relative velocity and the gas volume fraction are calculated using Eqs. (27) and (28) with the radial pressure gradient evaluated with Eq. (31). The liquid velocity, turbulence quantities and the axial pressure gradient are known for this process, taken from the last solution or from the initial guess. As the liquid volume fraction is present in Eq. (31), iterations are necessary to satisfy the input gas superficial velocity for each group.

Once the gas volume fraction and relative velocity are determined, the liquid velocity, k and ε are calculated with Eqs. (29), (32) and (33). Non-simultaneous solution of the k and ε equations require iterations, also necessary to evaluate the boundary conditions.

The boundary conditions were calculated using the already described two-phase logarithmic law. The process begins with a guess distance from the wall y_{lim} where the boundary conditions are evaluated. In order to calculate the shear stress, the liquid velocity derivative is determined in y_{lim} using Eq. (29) with the turbulence quantities taken from the last solution or from the initial guess. It can be noted that is not necessary to evaluate the liquid velocity profile at this point. Next, u^* is calculated with Eq. (42) and after that y^+, u_l, k and ε are calculated in y_{lim} with Eqs. (38)–(41).

Once the boundary conditions are determined, the liquid velocity profile and the profiles of k and ε are calculated. The liquid velocity can be evaluated using a forward elimination

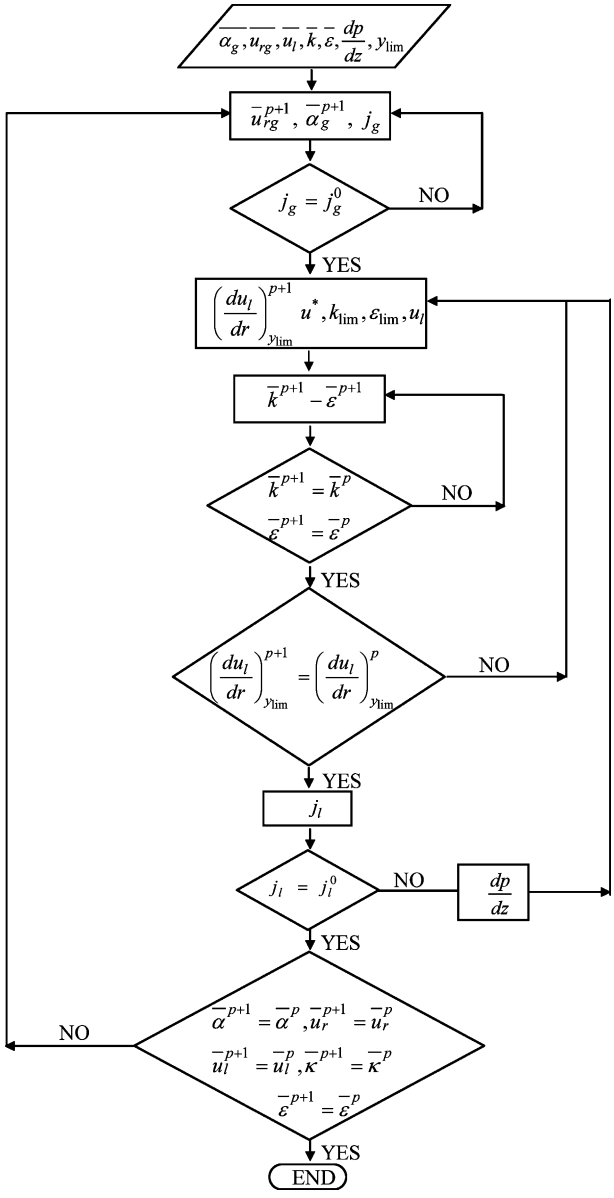

Fig. 2. Flow chart of the iterative solution procedure.

and backward substitution procedure in a non-iterative process. To avoid global instability in the calculation of the profiles of k and ε, we employed positive values for the turbulent viscosity and the coefficients of Eqs. (32) and (33), which may become temporarily negative during the iterative process and inhibit convergence (Lew et al., 2001). After the k–ε model converges, the shear stress and the boundary conditions are again calculated until the global convergence is obtained.

Known the liquid velocity and liquid volume fraction profiles, the liquid superficial velocity is verified. If the liquid superficial velocity is not satisfied the pressure axial gradient is modified and the calculus of liquid velocity, boundary conditions and the k–ε model are repeated. Unfortunately, axial pressure gradient was not reported in the available experimental data.

The turbulence near the wall is calculated with Eqs. (43) and (44). Finally, the condition $30 \leqslant y^+ \leqslant 100$ is verified.

3.5. Comments about the model

The set of constitutive equations and boundary conditions presented herein contain most of the relevant physical mechanisms of the two-phase flow described. Given the complexity of the phenomena, the simplest modeling was used as long as it captured the global physics of the process. Near the wall, other mechanisms are present that are not included in this model due to the simplifications used. Particularly, when the bubbles are concentrated near the wall the models used for the turbulent kinetic energy and dissipation bubbles sources are not valid because they were deduced assuming potential flow around a single sphere with no consideration to bubble–bubble interaction, deformation due to shear stress near the wall, etc. In addition, several of the forces acting on the bubbles were derived assuming homogeneous flow, a condition that is not fulfilled near the wall, were the length scales can be much smaller than the bubble size. Besides, the use of the same constants as in single flow for the k–ε model and the near-wall logarithmic law are only justified by the behavior of the two-phase flow model when the gas volume fraction tends to zero.

The interfacial force terms should also be modeled more carefully near the wall. The turbulent dispersion model used, though appropriate for essentially constant Stokes number flows (Moraga et al., 2001), may require improvement for the case of interaction with large turbulent structures (Tran-Cong et al., 2001). The drag coefficient, Eq. (7), was derived for the case of unbounded flows and is not necessarily applicable near a solid wall. Similar discussion is valid for other interfacial forces.

Furthermore, the two-phase logarithmic law presented here assumes that both the turbulent kinetic energy and the gas volume fraction are constant between $30 \leqslant y^+ \leqslant 100$. This could be an even stronger assumption than in single-phase flow, and no experimental evidence supports this statement.

Another important point is that the calculation of the gas volume fraction requires k and ε near the wall as input. In this work we modeled the near-wall turbulence studying the asymptotic behavior of the solution of model k–ε. This turbulence model changes with the selection of the distance y^+_{lim} where the boundary conditions are evaluated.

Because of the above-mentioned causes, the gas volume fraction distribution depends on the distance to the wall y^+_{lim} where the k–ε boundary conditions are evaluated. While y^+_{lim} increases, the peak of gas volume fraction near the wall decreases. According to the numerical results an increase of y^+_{lim} is equivalent to a diffusion term. Fig. 3 shows the sensitivity of the liquid and gas velocity profiles to different choices of y^+_{lim}, both for the case of the two-phase log-law and the single-phase log-law, for the case of the experiment of Liu and Bankoff (1993a) with $j_{\mathrm{l}} = 0.753$ m/s and $j_{\mathrm{g}} = 0.23$ m/s. Even though the velocity profiles have a small change using the proposed two-phase log-law, as compared to the case using the single-phase log-law, the gas volume

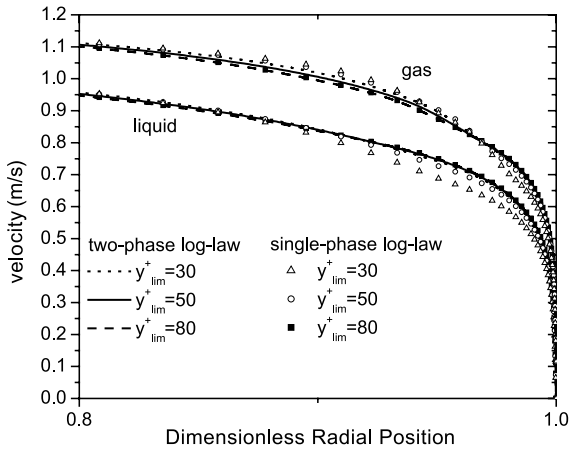

Fig. 3. Effect of the selection of y^+_{lim} on the velocity profiles.

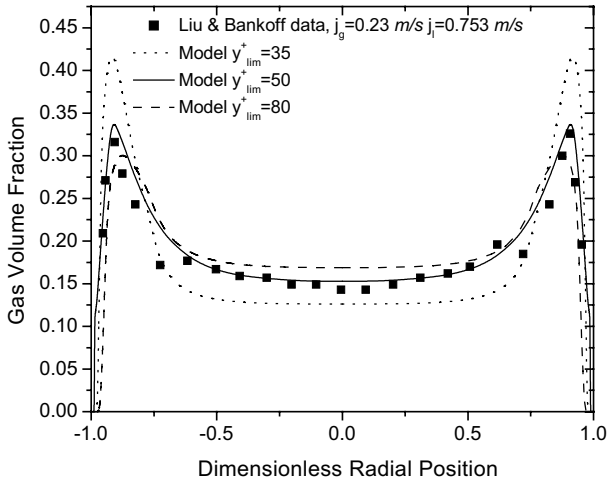

Fig. 4. Effect of the selection of y^+_{lim} on the gas volume fraction profile.

fraction is sensible to these small variations in velocity profile, due to the large change in the velocity gradient at the wall. The effect of the choice of y^+_{lim} on the gas volume fraction distribution is shown in Fig. 4, compared against the data of Liu and Bankoff (1993b). It is clear that y^+_{lim} still has a large effect on the gas distribution, and that a larger y^+_{lim} tends to have a diffusive effect. In this work the distance y^+_{lim} was a control parameter to fit the experimental data. This point is the principal drawback of the proposed model. Clearly, more elaborated models are necessary in the near-wall region.

Even with the limitations mentioned, the numerical results of the polydisperse two-phase model fit reasonably well the experimental data. With the correction of the logarithmic law for two-phase flow the liquid velocity profile does not change with the selection of y^+_{lim}, as occurs with the standard k–ε model (Lopez de Bertodano et al., 1994). This is a considerable advantage

comparing to the use of the standard single-phase flow k–ε model, because if the liquid velocity profiles changes, the lift force, the turbulent dispersion and other processes forces over the bubbles are modified and the gas volume fraction profile is completely different every time y^+_{lim} is changed.

4. Results

The model was compared against the experimental data measured by Serizawa et al. (1975a,b), Zun (1990), Liu and Bankoff (1993a,b), Liu and Wang (2001) and Liu (1998) in air/water vertical ducts. To simulate the experiments the duct was discretized in 52 radial nodes with continuous finer discretization near the wall (25 nodes from $r/R = 0.98$ to $r/R = 1$), where the variables have the largest variations. As a first representation, the bubble mass was discretized in three groups. These three groups can be selected with any size, in particular all can be of the same diameter for single-bubble size runs, or can simulate bimodal distributions.

The distance where the boundary conditions were evaluated was an adjustable parameter. The range used to do the simulations was $50 < y^+_{\text{lim}} < 55$, and it was used for all the experiences.

The shear stress data by Liu (1997) in a circular pipe 0.0572 m inner diameter were used to test the proposed two-phase log-law. Fig. 5 shows the model predictions and the experimental data for $j_g = 0.1$ and 0.2 m/s and for $j_j = 1$ and 4 m/s, with j_j the superficial velocity of a liquid jet flowing through the bubble injector and that determines the size of the bubbles. The single-phase shear stress is also included in Fig. 5. We note that the model tends to correct the shear stress towards the experimental value, though underpredicts the shear stress for low gas superficial velocities. The more elaborate model of Troshko and Hassan (2001b, see Figs. 28–30) do a slightly better job, but still tends to underpredict the shear stress.

4.1. Experimental data of Serizawa et al. (1975a,b)

The gas volume fraction and liquid velocity profiles predicted by the model are compared with the experimental data of Serizawa et al. (1975b) in a bubble column of 0.06 m internal diameter and 2.1 m long. The bubble radius used for the simulations was the reported by the authors, $r_g = 0.002$ m.

The authors measured the gas volume fraction with a resistive probe 0–2 mm in diameter, with a sampling time of 1–3 min. Hot film anemometry was used to measure the liquid velocity profiles. The fully-developed flow was obtained in a dimensionless axial position $z/R_c = 60$.

The results, for gas superficial velocity $j_g = 0.215$ m/s and liquid superficial velocity $j_l = 1.03$ m/s, are shown in Figs. 6 and 7. The gas volume fraction presents a peak near the wall, due to the lift force that cause the migration of small bubbles towards wall. This already "classic" behavior has been modeled by Lopez de Bertodano et al. (1994). These authors used the lift coefficient as adjustable parameter to obtain a reasonable fit of the experimental data. The turbulent energy production, calculated by Eq. (20), is compared with the experimental data shown by Serizawa et al. (1975b) in Fig. 8. As shown by the figures, the agreement of the model with the data is satisfactory.

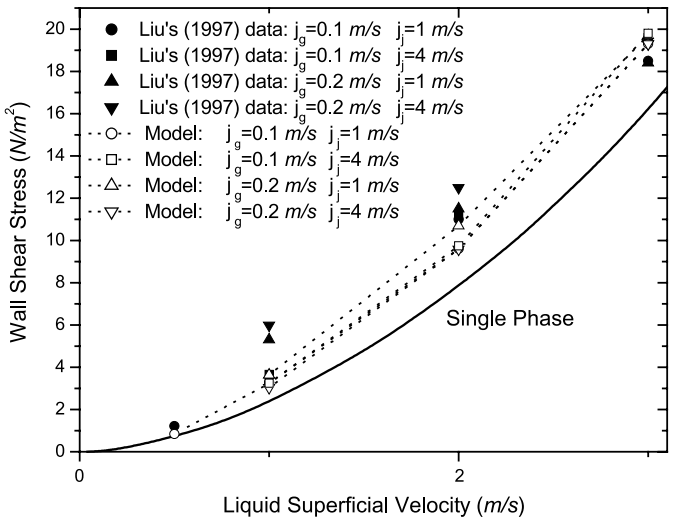

Fig. 5. Comparison of the wall shear stress predicted by the model with experimental data.

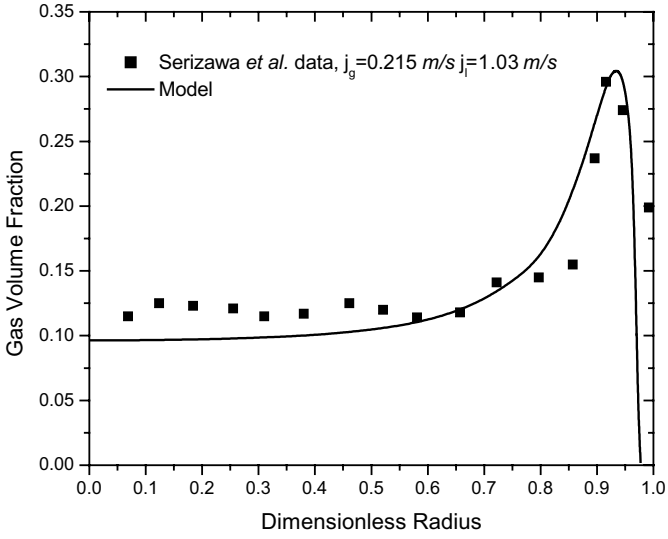

Fig. 6. Gas volume fraction profile for $j_g = 0.215$ m/s and $j_l = 1.03$ m/s. Model (curve) and experimental data of Serizawa et al. (1975b) (symbols).

4.2. Experimental data of Zun (1990)

Zun measured the gas volume fraction profile by microresistivity probes of 0.011 mm tip diameter, in a square-section channel, 0.254 m inside, for a liquid superficial velocity $j_l = 0.43$ m/s. Two separated single nozzles were used to generate air bubbles of two different well-controlled sizes.

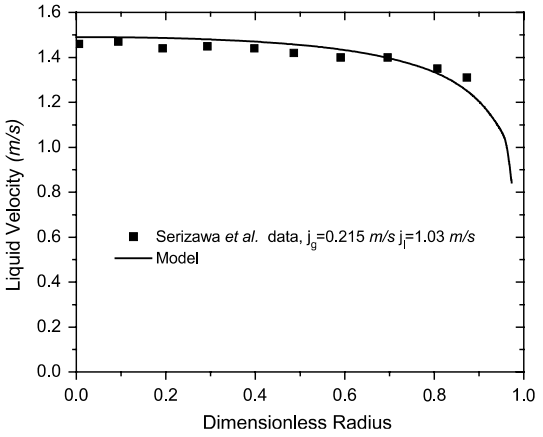

Fig. 7. Liquid velocity profile for $j_g = 0.215$ m/s and $j_l = 1.03$ m/s. Model (curve) and experimental data of Serizawa et al. (1975b) (symbols).

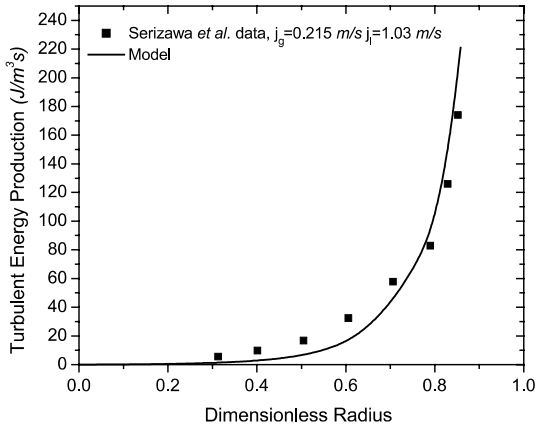

Fig. 8. Turbulent energy production profile for $j_g = 0.215$ m/s and $j_l = 1.03$ m/s. Model (curve) and data of Serizawa et al. (1975b) (symbols).

The low liquid superficial velocity causes an important error in the simulation of the turbulence because the near-wall logarithmic, buffer and laminar zones take up an important part of the duct. As the author did not report the gas superficial velocity, j_g was used as an adjustable parameter to obtain the agreement between the experimental data and the model.

Fig. 9 compares the model results with the experimental data. The simulation was performed with the bubble sizes measured by the author $r_g = 0.00205$ m, $r_g = 0.0032$ m and a combination of these two sizes. It can be noted that the gas volume fraction profiles change markedly with the bubble size. For bubbles with $r_g = 0.00205$ m the gas volume fraction shows a peak at the wall, while that for bubbles with $r_g = 0.0032$ m the gas volume fraction profile have convex shape. This behavior can be explained considering that the smaller bubbles accumulate near the wall while the

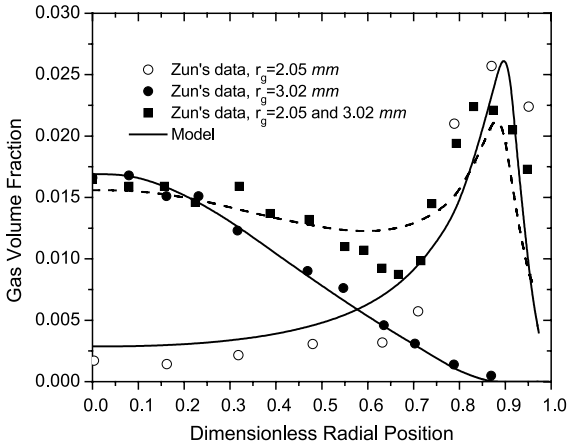

Fig. 9. Gas volume fraction profile for $j_l = 0.43$ m/s. Model (curves) and data of Zun (1990) (symbols).

bigger ones tend to concentrate at the center of the tube. In the model this behavior is caused by the change in sign of the lift coefficient beyond a critical size.

The model is also capable to predict the double peak observed when the bubbles have two distinct different sizes. It is important to note that the resulting gas volume fraction is not the sum of the effect of each size considered isolated since the liquid velocity, the turbulence and the radial pressure gradient depends on the total gas volume fraction. Therefore the correct way to simulate these flows is with a polydisperse model that considers different bubble sizes simultaneously, in a two-way coupling between the gas and liquid equations.

Figs. 10 and 11 show the importance of the different bubble lateral force terms for the cases considered in this section. Plotted are the lift force (Eq. (8)), turbulent dispersion (Eq. (15)), wall

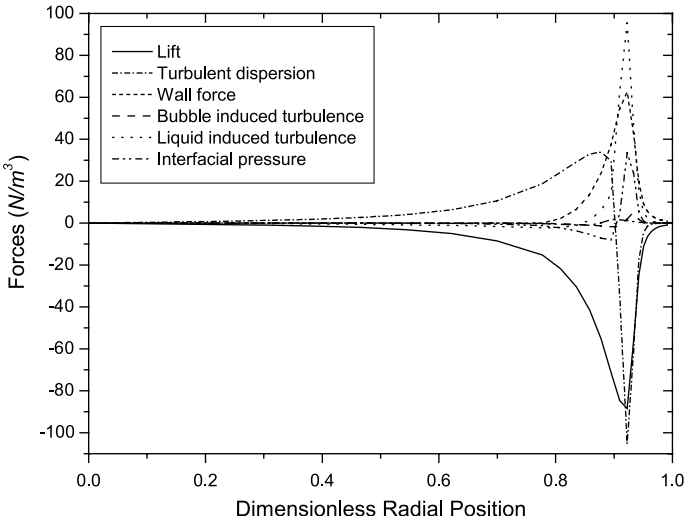

Fig. 10. Radial forces predicted by the model for Zun's case with $r_g = 0.00205$ m.

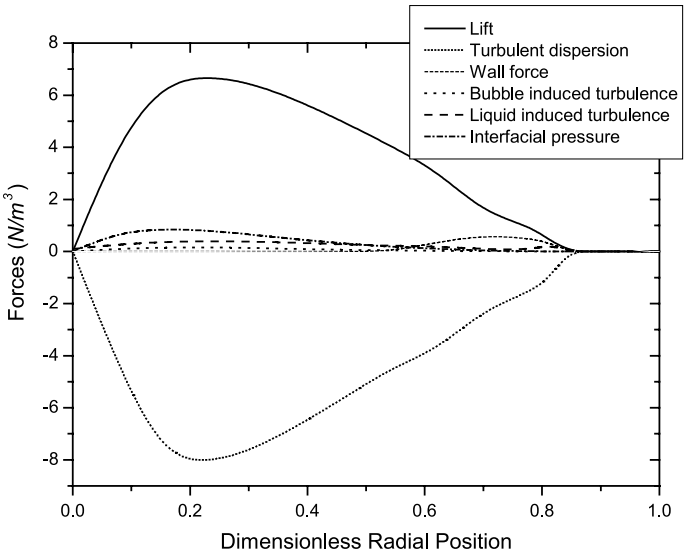

Fig. 11. Radial forces predicted by the model for Zun's case with $r_g = 0.0032$ m.

force (Eq. (13)) and pressure force. The pressure force (Eq. (31)) has been split into liquid induced turbulence (first RHS term), bubble induced turbulence (second RHS term), and interfacial pressure (rest of the RHS). For small bubbles (Fig. 10), the near wall forces are dominant, mainly the lift, wall and turbulent forces. It is interesting the change in sign of the turbulent dispersion term at the peak in gas volume fraction. For large bubbles (Fig. 11) the lift and turbulent dispersion forces, and to a less extent pressure forces, are the main contributions to the force balance.

Another interesting point is that the model agrees better with the behavior of large bubbles than for small bubbles. This could be due to a better work of the proposed turbulence model when there is no wall peaking in the gas volume fraction.

4.3. Experimental data of Liu and Bankoff (1993a,b)

Liu and Bankoff (1993a,b) measured the radial profiles of gas volume fraction and liquid and bubble velocities using hot-film anemometer probes and a dual-sensor resistivity probe of about 0.005–0.008 mm tip diameter. The test section was a vertical duct, 2.8 m long, 0.038 m inner diameter. The bubble generator had 64 equally-spaced needles of 0.1 mm diameter at the upper part of the inlet plenum, to obtain a uniform size distribution of small bubbles with 0.002–0.004 m mean diameter.

The model results, for bubbles with $r_g = 0.0015$ m, gas superficial velocity $j_g = 0.23$ m/s and liquid superficial velocity $j_l = 0.753$ m/s, are compared with the experimental data of Liu and Bankoff (1993b) in Figs. 4 and 12. In this case the numerical results shown a good agreement with the experimental data except near the wall where the measured velocities are bigger than those predicted by the model. These differences can be due to some error reporting the experimental data, because the experimental liquid velocity at the wall is not zero, a condition that the model

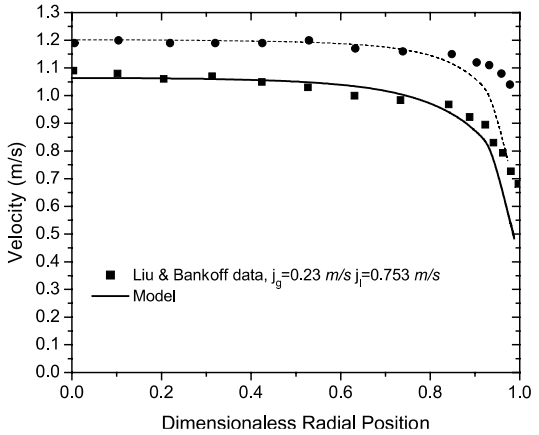

Fig. 12. Profiles of liquid and gas velocities. Model (curves) and experimental data of Liu and Bankoff (1993b) (● gas velocity and ■ liquid velocity).

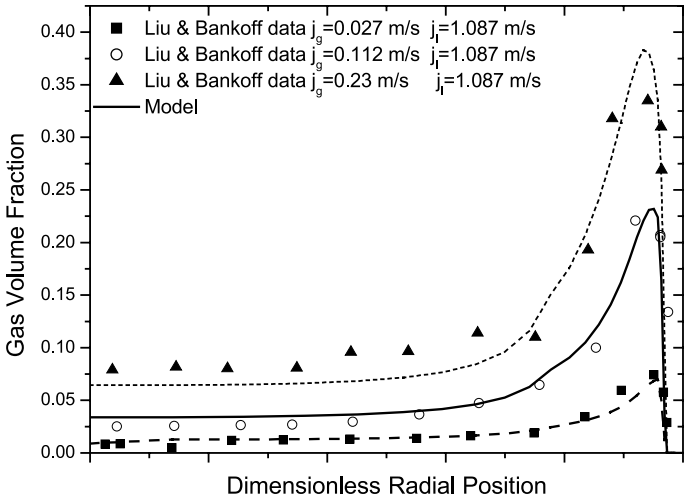

Fig. 13. Gas volume fraction profile by the model (curves) for the experimental conditions measured by Liu and Bankoff (1993b) (symbols).

always meets. In addition, the drag coefficient of Eq. (7), which plays an important role to calculate the drift velocity, is appropriate for unbounded bubbles and therefore inaccurate near the wall.

We include in Fig. 13 data for $j_l = 1.087$ m/s, $j_g = 0.027, 0.112, 0.23$ m/s to show the ability of the model to predict the change on the peak in gas volume fraction for different gas superficial velocities. Though the trend is correct, the model tends to slightly overpredict the peak at high gas superficial velocities and underpredict for low superficial velocities.

4.4. Experimental data of Liu and Wang (2001)

Liu and Wang (2001) measured the profiles of gas volume fraction, bubble impact rate and bubble mean diameter, for different gas and liquid superficial velocities in a bubble column, 8 m long and 0.0572 m inner diameter. The resistivity probe used was the same previously reported by Liu (1991) and by Liu and Bankoff (1993b).

The bubble size was controlled by a bubble generator in which compressed air was injected through a sintered cylinder into the water and was sheared away by a high speed water jet (Liu, 1991). The bubble size was controlled by setting the nozzle liquid jet superficial velocity j_j. As reported by Liu and Wang (2001), the bubble size depends also on the axial distance to the injection point, which means that this experiment is not fully developed, probably due to an incomplete migration of bubbles towards the center or wall of the pipe, or due to breakup-coalescence phenomena. Unfortunately, the authors only report mean bubble sizes at the measurement station, $L/D = 60$, and not bubble size distributions, which would have provided less degrees of freedom to fit the experimental data. Therefore the bubble size distribution at the inlet was guessed such that the total j_g is satisfied and that the mean bubble size is honored. In addition, the shape of the distribution can be chosen and still satisfy the previous conditions, so the final choice was made to obtain a good agreement with the experimental data. The distributions used in this case are reported in Table 1.

The bubble impact rate is the number of bubbles that touch the tip of the resistivity probe in one second. In order to compare with the experimental data, the model bubble impact rate, f_i, was calculated using the expression proposed by Sanz et al. (1995):

$$f_i = \frac{3}{4} \sum_{g=1}^{N} \frac{\varepsilon_g u_g}{r_g} \tag{45}$$

The local mean bubble size reported by Liu and Wang (2001) was determined from the measurements of the bubble chord length, based on statistical processing of the bubble residence time in gas, assuming that the bubbles are spherical and that the bubble motion is unidirectional. With the model variables, the mean bubble diameter, $\bar{d}_b$, was evaluated with the expression:

$$\bar{d}_b = \frac{3}{2} \frac{\sum_{g=1}^{N} \varepsilon_g u_g}{f_i} \tag{46}$$

Table 1
Size distributions used for the experiments of Liu and Wang (2001)

j_j (m/s)	j_g (m/s)	
	0.1	0.2
1	40% (3.0 mm) 60% (7.0 mm)	40% (4.0 mm) 60% (8.0 mm)
4	35% (3.0 mm) 50% (4.0 mm) 15% (6.5 mm)	35% (4.5 mm) 50% (5.0 mm) 15% (7.5 mm)

Figs. 14 and 15 show the experimental data and the predictions of the model, for $j_l = 2$ m/s and gas superficial velocities $j_g = 0.2$ m/s and $j_g = 0.1$ m/s in a dimensionless axial position $z/R_c = 60$. The open symbols represent flows with low nozzle jet velocity ($j_j = 1$ m/s) and big bubbles while that the solid symbols correspond to high nozzle jet velocity ($j_j = 4$ m/s) where the bubble size is reduced drastically and the bubbles are distributed more uniformly in the duct.

We can see that for smaller bubbles ($\bar{d}_b \approx 4$–5 mm) the gas volume fraction and the bubble impact rate present a peak near the wall representing that the largest part of the bubbles are pushed against the wall. When the bubble size distribution has simultaneously big and small bubbles a second peak develops at the center of the duct, and the peak near the wall decreases correspondently, as already reported in the measurements by Zun (1990).

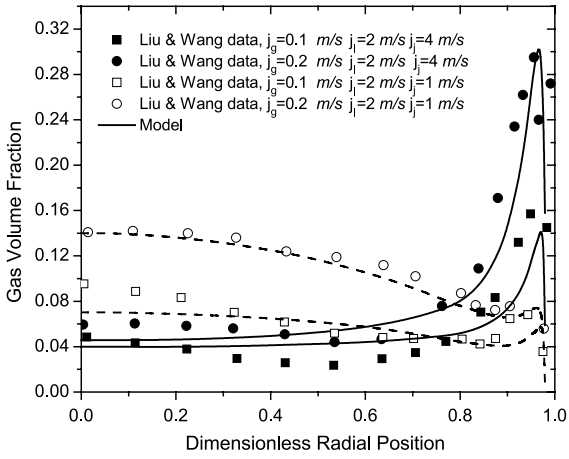

Fig. 14. Gas volume fraction profiles. Model (curves) and experimental data of Liu and Wang (2001) (symbols).

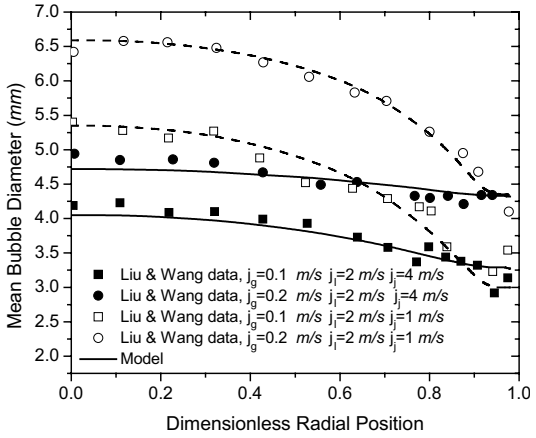

Fig. 15. Mean bubble diameter profile. Model (curves) and experimental data of Liu and Wang (2001) (symbols).

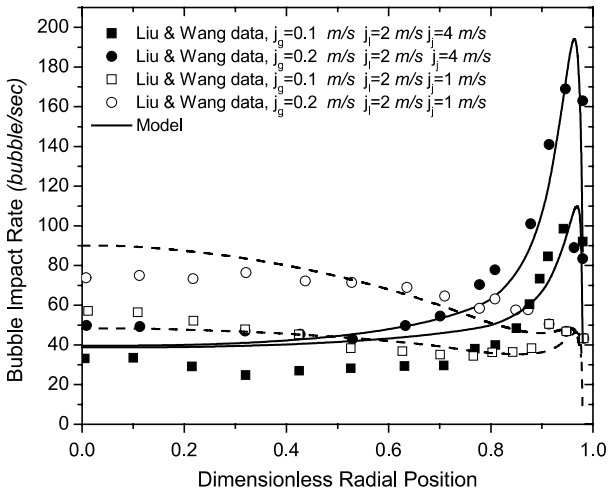

Fig. 16. Bubble impact rate profiles. Model (curves) and experimental data of Liu and Wang (2001) (symbols).

Notice that the gas volume fraction and bubble impact rate peaks near the wall are well represented by the model, as well as the behavior of the gas volume fraction and bubble impact rate profiles for large and small bubbles. The mean bubble diameter is also properly predicted.

It is possible to note in the experimental data in Fig. 16 a trend to get slightly larger bubbles at the wall. This behavior cannot be predicted by the model, and could be caused by bubble coalescence near the wall, and/or bubble elongation due to shear stress, which would produce an experimentally larger bubble chord. Should these bubbles be really larger, they would migrate toward the center of the channel, while the small bubbles arising from bubble breakup will migrate toward the wall. This effect can also be noted in the data measured by Liu (1998), discussed on the next section. The inclusion of bubble breakup and coalescence is necessary in order to get a model able to predict such a behavior. This improvement of the model is left for a future paper.

4.5. Experimental data of Liu (1998)

The experimental data by Liu (1998) provide an opportunity to test the model against turbulence data. This has already been recognized by Troshko and Hassan (2001b), who compare their model of bubbly flow turbulence against this set of data. The experimental setup is described in detail in their paper and is similar to the system used by Liu and Wang (2001) already reported in Section 4.4.

We use the data for $j_g = 0.1$ m/s, $j_l = 1$ m/s and $j_j = 0.5$ and 6 m/s, this last parameter already defined in Section 4.4 and used to change the bubble size. In Fig. 17 we show a comparison of the predicted average bubble diameter with the experimental data for the cases of large and small bubbles. Also as a reference, the single size used by Troshko and Hassan (2001b) is included. A good fit is obtained with the exception of a region where the model underpredicts the

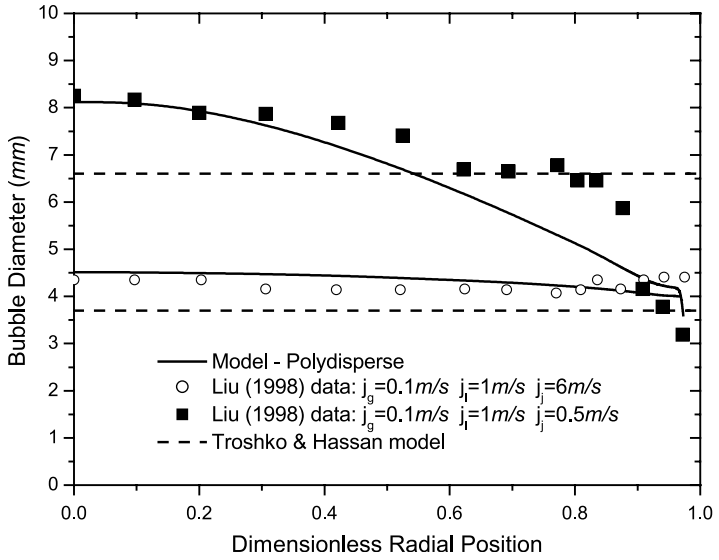

Fig. 17. Mean bubble diameter profiles predicted by the model compared against the experimental data of Liu (1998) and the model of Troshko and Hassan (2001b) for the cases with large and small bubbles.

Table 2
Size distributions used for the experiments of Liu (1998)

j_j (m/s)	j_g (0.1 m/s)
0.5	25% (3.6 mm) 17% (5.5 mm) 58% (10.2 mm)
6	75% (4.0 mm) 25% (12.5 mm)

bubble size near $r/R = 0.75$. The bubble sizes distributions used in this set of data are reported in Table 2.

Figs. 18–20 show the gas volume fraction, liquid velocity and the rms of the axial liquid velocity fluctuations for the case of $j_j = 6$ m/s. In all the figures the experimental data, the model by Troshko and Hassan (2001b) and the results of the present model with uniform size (same as Troshko and Hassan) and polydisperse are shown. It is clear that the polydisperse model obtains a better match than the single size model for all the variables tested. The liquid velocity near the wall is better matched in the model by Troshko and Hassan (2001b), but at the core of the duct the present model shows much better results. The axial turbulence is also better matched by the polydisperse model. Near the wall all models give very similar results.

The data in Fig. 18 shows a trend to accumulate bubbles at the center of the duct. Our polydisperse model can only follow that trend with large bubbles, so a better match can be obtained increasing the amount of large bubbles on the size distribution. Similarly, the data shows

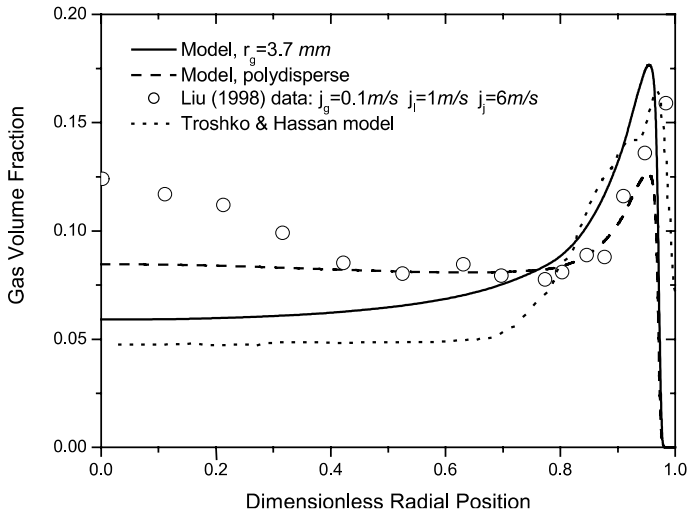

Fig. 18. Gas volume fraction profiles predicted by the model compared against the experimental data of Liu (1998) and the model of Troshko and Hassan (2001b) for the case of small bubbles.

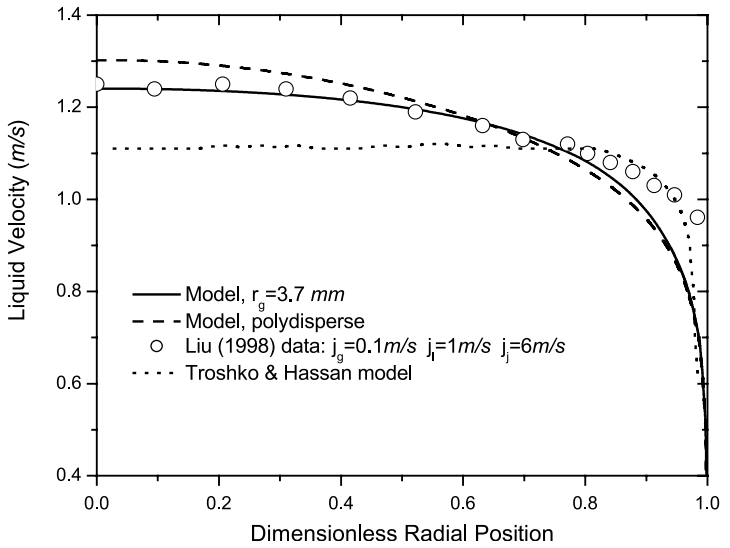

Fig. 19. Liquid velocity profiles predicted by the model compared against the experimental data of Liu (1998) and the model of Troshko and Hassan (2001b) for the case of small bubbles.

larger gas volume fraction at the wall than the one achieved by the model. Though the gas volume fraction data can be much better matched changing the size distribution, the average radius reported in Fig. 17 cannot be matched. Reason for this inconsistency can be bubble elongation and/or coalescence near the wall or a non-fully-developed flow.

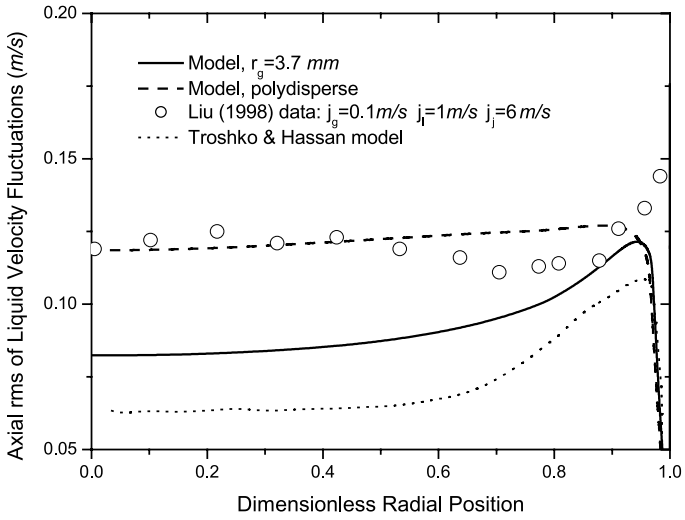

Fig. 20. Profiles of the RMS axial liquid velocity fluctuations predicted by the model compared against the experimental data of Liu (1998) and the model of Troshko and Hassan (2001b) for the case of small bubbles.

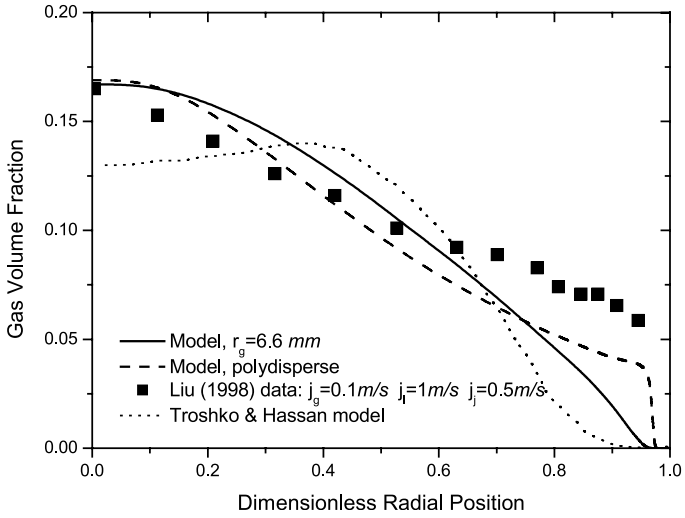

Fig. 21. Gas volume fraction profiles predicted by the model compared against experimental data of Liu (1998) and model of Troshko and Hassan (2001b) (case of large bubbles).

The model is compared with experimental data of gas volume fraction, liquid velocity and the rms of the axial liquid velocity fluctuations for the case of large bubbles in Figs. 21–23. Again, the polydisperse model does a better job than both single-size models predicting all the variables. However, the models tend to underpredict the gas volume fraction at the wall, though a clear improvement in that region is obtained by the polydisperse model. Also, as in the case of small bubbles, the model tends to underpredict the liquid velocity near the wall. This can be caused by the underprediction of the wall shear stress by the model, as shown in Fig. 5.

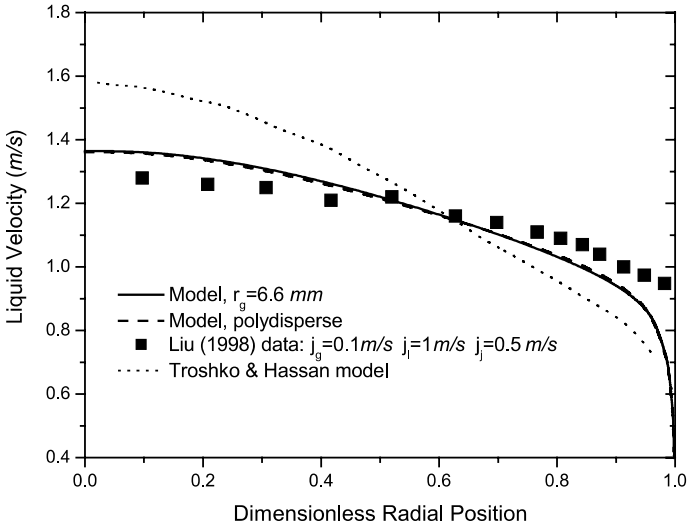

Fig. 22. Liquid velocity profiles predicted by the model compared against the experimental data of Liu (1998) and the model of Troshko and Hassan (2001b) for the case of large bubbles.

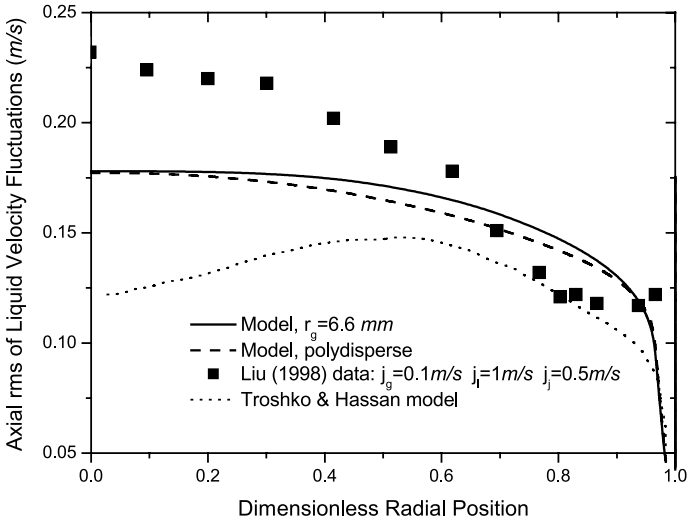

Fig. 23. Profiles of the RMS axial liquid velocity fluctuations predicted by the model compared against the experimental data of Liu (1998) and the model of Troshko and Hassan (2001b) for the case of large bubbles.

5. Conclusions

A two-phase flow model has been developed to study the bubble size effect on the radial gas distribution in a vertical upward duct. The formulation is based on the two-fluid model for two-phase flow. A polydisperse approach was used to represent the bubble size distribution. The model was numerically solved for steady-state, fully developed flow with a finite differences

method. The k–ε model, modified for two-phase flow, was used to calculate the turbulence parameters. The boundary conditions near the wall were evaluated with a wall law adapted for two-phase flow. Near the wall the turbulence was calculated considering the asymptotic behavior of k–ε model approaching a solid surface. With the proposed model the velocity profile does not change with the distance from the wall where the boundary conditions are evaluated, y_{lim}. However, the height of the peak of the gas volume fraction is modified with y_{lim}, probably due to the assumptions necessary to obtain a simple meaningful model. Even with these drawbacks, the two-phase boundary conditions perform better than the standard k–ε boundary conditions.

The model was compared against the experimental data of Serizawa et al. (1975a,b), Zun (1990), Liu and Bankoff (1993a,b), Liu (1998) and Liu and Wang (2001) in air/water flows in vertical ducts. Good qualitative agreement was found and a reasonable quantitative fit was achieved with reasonable assumptions.

The results indicate that a better understanding of the basic mechanisms influencing the bubble behavior is still required. Particularly, it is necessary to develop models that consider interaction between bubbles of different sizes in turbulent flows. Furthermore, the turbulence near the wall requires a detailed investigation in order to allow a reliable prediction of the turbulent viscosity in this region in presence of bubbles. The effect of the presence of the wall in the drag, lift and other forces is not included in the model. In addition, the model is limited to low gas and liquid superficial velocities where bubble breakup and coalescence can be neglected. Future work including these phenomena will allow the prediction of a radial flow of bubbles of different sizes and the evolution of the size distribution and regime transitions along the duct. The analysis presented herein seems to indicate that proper modeling of the turbulence, mainly near the wall, is to be the most important improvement to the model at this stage.

Even though the above-mentioned problems have yet to be solved, this study presents a model able for the first time to predict the change of behavior in the radial phase distribution in a turbulent two-phase flow in a vertical duct when different bubble size distributions are present.

Acknowledgements

The authors wish to acknowledge the financial support for Marcela Politano through a CONICET graduate student fellowship.

References

Antal, S.P., Lahey Jr., R.T., Flaherty, J.E., 1991. Analysis of phase distribution in fully developed laminar bubbly two-phase flow. Int. J. Multiphase Flow 17, 635–652.

Carrica, P.M., Drew, D., Bonetto, F., Lahey Jr., R.T., 1999. A polydisperse model for bubbly two-phase flow around a surface ship. Int. J. Multiphase Flow 25, 257–305.

Drew, D.A., Lahey Jr., R.T., 1979. Application of general constitutive principles to the derivation of multidimensional two-phase flow equation. Int. J. Multiphase Flow 5, 243–264.

Drew, D.A., Passman, S.L., 1998. Theory of Multicomponent Fluids. Springer, New York.

Ishii, M., 1975. Thermo-fluid dynamic theory of two-phase flow. Eyrolles, Paris.

Ishii, M., Mishima, K., 1984. Two fluid model and hydrodynamic constitutive relations. Nucl. Eng. Des. 82, 107–126.
Ishii, M., Zuber, N., 1979. Drag coefficient and relative velocity in bubbly, droplet or particulate flows. AIChE J. 25, 843–855.
Lahey, Jr., R.T., Drew, D.A., 1999. The analysis of two-phase flows and heat transfer using a multidimensional, four field, two-fluid model. In: 9th International Meeting on Nuclear Reactor Thermal-Hydraulics, Rensselaer Polytechnic Institute, NY.
Lamb, H., 1932. Hydrodynamics. Cambridge University Press, Cambridge, UK.
Lee, S.J., Lahey Jr., R.T., Jones, O.C., 1989. The prediction of two-phase flow turbulence and phase distribution using a κ–ε model. Jpn. J. Multiphase Flow 3, 335–368.
Lew, A.J., Buscaglia, G.C., Ferrari, H., Carrica, P.M., 2001. A note on the numerical treatment of the k–ϵ turbulence model. Int. J. Comp. Fluid Mechanics 14, 201–209.
Liu, T.J., 1991. The effect of bubble size on void fraction. Distribution in a vertical pipe. In: Proceedings of the Second International Conference on Multiphase Flows, Tsukuba, Japan.
Liu, T.J., Bankoff, S.G., 1993a. Structure of air–water bubbly flow in a vertical pipe. I: Liquid mean velocity and turbulence measurements. J. Heat Transfer 36, 1049–1060.
Liu, T.J., Bankoff, S.G., 1993b. Structure of air–water bubbly flow in a vertical pipe. II: Void fraction, bubble velocity and bubble size distribution. J. Heat Transfer 36, 1061–1072.
Liu, T.J., 1997. Investigation of the wall shear stress in vertical bubbly flow under different bubble size conditions. Int. J. Multiphase Flow 23, 1085–1109.
Liu, T.J., 1998. The role of bubble size on liquid phase turbulent structure in two-phase bubbly flow. In: Proceedings of the 3rd International Conference on Multiphase Flow ICMF'98, Lyon, France.
Liu, T.J., Wang, S.J., 2001. Optimization of local and area-averaged interfacial area concentration correlations in two-phase bubbly flow. In: Fourth International Conference on Multiphase Flow, New Orleans.
Lopez de Bertodano, M.A., Lahey Jr., R.T., Jones, O.C., 1994. Phase distribution in bubbly two-phase flow in vertical ducts. Int. J. Multiphase Flow 20, 805–818.
Marié, J.L., Moursali, E., Tran-Cong, S., 1997. Similarity law and turbulence intensity profiles in bubbly boundary layer at low void fractions. Int. J. Multiphase Flow 23, 227–247.
Moraga, F.J., Larreteguy, A.E., Drew, D.A., Lahey Jr., R.T., 2001. Assessment of turbulent dispersion models for bubbly flows. In: Fourth International Conference on Multiphase Flow, New Orleans.
Nakoryavok, V.E., Kashinsky, O.N., Randin, V.V., Timkin, L.S., 1996. Gas–liquid bubbly flow in vertical pipes. J. Fluids Eng. 118, 377–382.
Nigmatulin, R.I., 1979. Spatial averaging in the mechanism of heterogeneous and dispersed systems. Int. J. Multiphase Flow 4, 353–385.
Sanz, D., Guido Lavalle, G., Carrica, P., Clausse, A., 1995. About the statistical description of gas–liquid flows. In: 7th International Meeting on Nuclear Reactor Thermal–Hydraulics, Saratoga Springs, USA.
Sato, Y., Sadatomi, M., Sekoguchi, K., 1981. Momentum and heat transfer in two-phase bubble flow: I and II. Int. J. Multiphase Flow 7, 167–190.
Sekoguchi, K., Sato, Y., Honda, T., 1974. An experimental investigation on bubble flow: first report. Trans. Jpn. Soc. Mech. Eng. 40, 1395–1403 (in Japanese).
Serizawa, A., Kataoka, I., Michiyoshi, I., 1975a. Turbulence structure of air–water bubbly flow. I: Measuring techniques. Int. J. Multiphase Flow 2, 221–233.
Serizawa, A., Kataoka, I., Michiyoshi, I., 1975b. Turbulence structure of air-water bubbly flow. II: Local properties. Int. J. Multiphase Flow 2, 235–246.
Tran-Cong, S., Marié, J.L., Perkins, R.J., Bubble migration in a turbulent boundary layer: The influence of coherent structures. In: Fourth International Conference on Multiphase Flow, New Orleans.
Tomiyama, A., 1998. Struggle with computational bubble dynamics. In: 3rd International Conference on Multiphase Flow. Lyon, France.
Troshko, A.A., Hassan, Y.A., 2001a. Law of the wall for two-phase turbulent boundary layers. Int. J. Heat Mass Transfer 44, 871–875.
Troshko, A.A., Hassan, Y.A., 2001b. A two-equation turbulence model of turbulent bubbly flows. Int. J. Multiphase Flow 27, 1965–2000.

Wang, S.K., Lee, S.J., Jones Jr., O.C., Lahey Jr., R.T., 1987. 3-D Turbulence structure and phase distribution measurements in bubbly two-phase flows. Int. J. Multiphase Flow 13, 327–343.

Wellek, R.M., Agrawal, A.K., Skelland, A.H.P., 1966. Shapes of liquid drops moving in liquid media. AIChE J. 12, 854.

Wilcox, C., 1998. Turbulence Modeling for CFD. DCW Industries, California.

Zun, I., 1988. Transition from wall void peaking to core void peaking in turbulent bubbly flow. Int. J. Multiphase Flow 6, 583–588.

Zun, I., 1990. The mechanism of bubble non-homogeneous distribution in two-phase shear flow. Nucl. Eng. Des. 118, 155–162.